J. Fluid Mech. (2005), *vol.* 536, *pp.* 377–400.
doi:10.1017/S0022112005005100 Printed in the United Kingdom

Acoustic receptivity of the boundary layer over parabolic bodies at angles of attack

By O. M. HADDAD[1], E. ERTURK[2] AND T. C. CORKE[3†]

[1]Department of Mechanical Engineering Jordan University of Science & Technology, PO Box 3030, Irbid 22110, Jordan
haddad@just.edu.jo

[2]Gebze Institute of Technology, Energy Systems Engineering Department, Gebze, Kocaeli 41400, Turkey
ercanerturk@eng.bahcesehir.edu.tr

[3]Department of Aerospace and Mechanical Engineering, University of Notre Dame, Notre Dame, IN 46556, USA
tcorke@nd.edu

(Received 7 April 2004 and in revised form 28 February 2005)

The effect of angle of attack on the acoustic receptivity of the boundary layer over two-dimensional parabolic bodies is investigated using a spatial solution of the Navier–Stokes equations. The free stream is decomposed into a uniform flow with a superposed periodic velocity fluctuation of small amplitude. The method follows that of Haddad & Corke (1998) and Erturk & Corke (2001) in which the solution for the basic flow and linearized perturbation flow are solved separately. Different angles of incidence of the body are investigated for three leading-edge radii Reynolds numbers. For each, the angle of attack ranges from 0° to past the angle where the mean flow separates. The results then document the effect of the angle of incidence on the leading-edge receptivity coefficient (K_{LE}), and in the case of the mean flow separation, on the amplitude of Tollmien–Schlichting (T-S) waves at the linear stability Branch II location (K_{II}). For angles of attack before separation, we found that the leading-edge receptivity coefficient, K_{LE}, increased with angle of incidence which correlated with an increase in the pressure gradient at the physical leading edge. When a separation zone formed at larger angles of incidence, it became a second site of receptivity with a receptivity coefficient that exceeded that of the leading edge. This resulted in dramatic growth of the T-S waves with Branch II amplitudes more than 100 times larger than those at angles just before separation, and 1000 times more than those at 0° angle of attack.

1. Introduction

Transition from laminar flow to turbulent flow is still one of the most fundamental and important problems in fluid mechanics. In a boundary layer, it has a key technological impact because it ultimately governs quantities such as skin friction and heat transfer. The transition process begins when disturbances enter from the free stream and excite instability modes within the boundary layer. At this stage, the process is referred to as 'receptivity'. For a Blasius flow, these instability modes are the Tollmien–Schlichting (T-S) modes provided the free-stream turbulence level is sufficiently

† Author to whom correspondence should be addressed.

low. In predicting the transition location, it is essential to know the initial amplitudes of the T-S modes at the leading edge. The receptivity coefficient relates the initial T-S amplitude to that of the free-stream disturbance.

Receptivity phenomena can be classified into two groups: vortical receptivity and acoustic receptivity. Physically, they correspond to vorticity fluctuation and sound waves (of infinite wavelength), respectively. With vortical receptivity, vorticity fluctuation is convected by the free stream and is often referred to as a convecting gust. With acoustic receptivity, boundary-layer instability is excited by free-stream sound. The length and time scales of the disturbance of each group do not match with those of T-S waves simultaneously. Thus, in order for them to excite any T-S wave, a scale-conversion mechanism is required.

Generally, receptivity comes about through non-parallel mean flow effects that may arise either in the leading-edge region, or in some localized region due to a step or joint (Goldstein & Hultgren 1989). Goldstein (1983, 1985) developed the earliest asymptotic analysis for localized receptivity on a semi-infinite zero-thickness plate. There are two general classes of receptivity regions recognized by Goldstein: (i) the leading-edge regions where the boundary layer is thin and growing rapidly; and (ii) regions further downstream where the boundary layer is forced to make a rapid adjustment such as when there are 'joints or bumps'.

Historically, two basic body shapes have been used to study receptivity. Murdock (1980), Haddad & Corke (1998), Erturk & Corke (2001) and Hammerton & Kerschen (1992, 1996) considered parabolic bodies. In this case the only site of receptivity was at the leading edge, and the pressure gradient is everywhere favourable. In the first two references, the receptivity coefficient was determined by numerically solving the unsteady Navier–Stokes (N-S) equations. Hammerton & Kerschen (1992, 1996) determined it using asymptotic methods.

The other shape which has been frequently used is an elliptic leading edge on a finite-thickness flat plate. This shape has more practical relevance in wind-tunnel experiments, and has been the subject of physical experiments by Shapiro (1977), Saric & Rasmussen (1992), Saric, Wei & Rasmussen (1994) and Saric & White (1998). The results of these motivated the N-S calculations of Lin, Reed & Saric (1990) and Fucciarelli (1997). The elliptic leading edge has an adverse pressure gradient, and two sites of receptivity, one at the leading edge and the other at the point where it joins the flat plate. To minimize the effect of the joint, Saric *et al.* (1994) used a 'modified super ellipse' (MSE). This used a variable exponent for the ellipse long axis to give zero curvature at the joint location. Wanderley & Corke (2001) performed N-S calculations for both elliptic and modified-ellipse leading edges of flat plates to simulate the conditions of Saric & White (1998). These exhibited the same frequency selection mechanism as observed in the experiments whereby the Branch I T-S amplitudes increased and decreased as the waves originating at the leading edge were 0° or 180° phase shifted to those originating at the downstream joint.

The analysis of Hammerton & Kerschen (1992, 1996, 1997), and the N-S simulations of Haddad & Corke (1998) and Erturk & Corke (2001) all found that the leading-edge receptivity coefficient increased as the leading-edge radius decreased, with the maximum receptivity occurring for an infinitely thin flat plate. When the receptivity values of Saric *et al.* (1994) and Fucciarelli (1997) were extrapolated upstream from Branch I to the leading edge, good quantitative agreement was found with the values of Haddad & Corke (1998) and Erturk & Corke (2001).

All of the previous literature on the flow over parabolic bodies has been at zero angle of incidence. In the last part of Haddad & Corke (1998), a preliminary look

at the effect of small angles of attack on the leading-edge receptivity coefficient was taken. These angles were well below ($\leqslant 7^\circ$) the point where flow separation would occur. Within this limited range, the leading-edge receptivity coefficient increased by as much as 65 % compared to zero angle of attack. The implications that this had on the T-S amplitudes at Branch II were not investigated.

Since all practical aerodynamic bodies are aerodynamically loaded, there is a natural interest in the full effect this has on boundary-layer instabilities. We expect this to be manifest through changes in the leading-edge receptivity coefficient, and in the linear stability growth rates that reflect changes in the mean flow resulting from favourable and unfavourable pressure gradients. An added effect comes when angles of attack are large enough to cause the flow to separate. This is expected to add another acoustic receptivity site similar to a surface bump or joint. Anecdotally, experimentalists studying boundary-layer instabilities on flat plates avoid leading-edge separation in order to maintain a suitable extent of laminar flow. The effect of even a small separation bubble is immediately detected through a dramatic decrease in the transition Reynolds number. Although this is commonly observed, to date there is no quantitative information about the acoustic receptivity of a closed separation bubble, and the degree to which it depends on other factors such as the wall geometry at or around the separation zone.

As part of a continued effort by the authors toward understanding the acoustic receptivity of the flow over parabolic bodies (e.g. Haddad & Corke 1998; Erturk & Corke 2001), the objective of this study is to investigate the effect of aerodynamic loading produced by orienting the body at a mean angle of attack. With this, the focus will be on both the leading-edge receptivity, and the receptivity that occurs owing to flow separations at large angles of attack. This will be investigated using the successful spatial formulation first introduced and applied to parabolic bodies by Haddad & Corke (1998) and Erturk & Corke (2001), as well as by Wanderley & Corke (2001) on elliptic leading edges of flat plates.

2. Physical problem

Figure 1 shows a diagram of the parabolic body set at a mean angle of attack with respect to a uniform flow. The equation of the surface of the parabolic body is given by

$$x(y) = \frac{1}{2R}\,(y^2 - R^2), \tag{1}$$

where x and y are the Cartesian coordinates, and R is the nose radius of curvature of the parabola.

2.1. *Governing equations*

In this study, the full N-S equations are considered. For a two-dimensional laminar incompressible flow, the N-S equations in streamfunction (ψ) and vorticity (ω) variables in the Cartesian coordinates are written in the form

$$\frac{\partial^2 \psi^*}{\partial x^{*2}} + \frac{\partial^2 \psi^*}{\partial y^{*2}} = -\omega^*, \tag{2}$$

$$\frac{\partial \omega^*}{\partial t^*} + \frac{\partial \psi^*}{\partial y^*}\frac{\partial \omega^*}{\partial x^*} - \frac{\partial \psi^*}{\partial x^*}\frac{\partial \omega^*}{\partial y^*} = \nu\left(\frac{\partial^2 \omega^*}{\partial x^{*2}} + \frac{\partial^2 \omega^*}{\partial y^{*2}}\right), \tag{3}$$

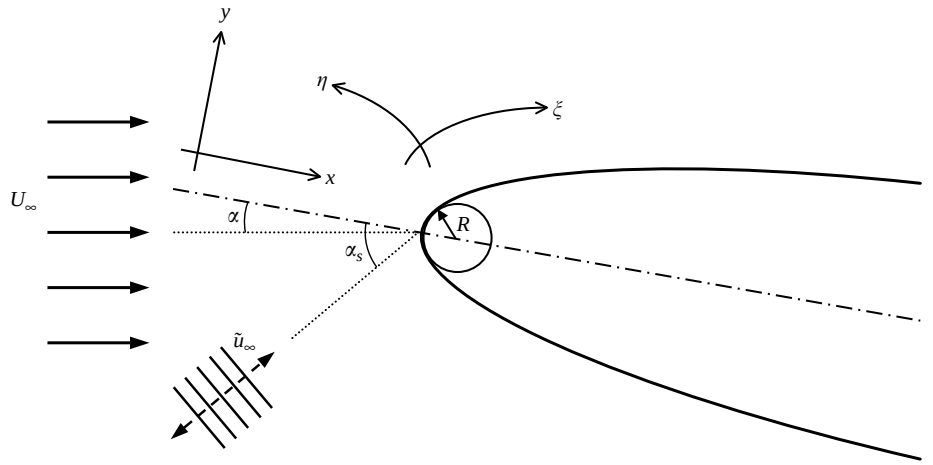

FIGURE 1. General schematic diagram of parabolic body at an angle of attack (α) in a uniform stream, and acoustic disturbance at an incident angle (α_s) with respect to body centreline.

where the superscript * denotes dimensional quantities. To non-dimensionalize the above equations, the free-stream velocity (U_∞) and viscosity (ν) are used such that

$$x = \frac{x^*}{\nu/U_\infty}, \quad y = \frac{y^*}{\nu/U_\infty}, \quad t = \frac{t^*}{\nu/U_\infty^2}, \quad \omega = \frac{\omega^*}{U_\infty^2/\nu}, \quad \psi = \psi^*/\nu. \tag{4}$$

In addition, the geometry of the body suggests that the problem be formulated in terms of parabolic coordinates. Among the advantages of using parabolic coordinates is that it allowed us to reduce any spurious receptivity that might have been produced by non-uniformities in the body contour or the numerical grid. The dimensionless parabolic coordinates (ξ, η) are related to the dimensionless Cartesian coordinates (x, y) by the following complex equation

$$x + \mathrm{i}y = \tfrac{1}{2}(\xi + \mathrm{i}\eta)^2 \tag{5}$$

or

$$x = \tfrac{1}{2}(\xi^2 - \eta^2), \quad y = \xi\eta. \tag{6}$$

Based on (4) and (6), the governing equations (2) and (3) can be non-dimensionalized and rewritten in parabolic coordinates as

$$\frac{\partial^2\psi}{\partial\xi^2} + \frac{\partial^2\psi}{\partial\eta^2} = -(\xi^2 + \eta^2)\,\omega, \tag{7}$$

$$-(\xi^2 + \eta^2)\,\frac{\partial\omega}{\partial t} + \frac{\partial^2\omega}{\partial\xi^2} + \frac{\partial^2\omega}{\partial\eta^2} + \frac{\partial\psi}{\partial\xi}\frac{\partial\omega}{\partial\eta} - \frac{\partial\psi}{\partial\eta}\frac{\partial\omega}{\partial\xi} = 0. \tag{8}$$

This is the final form of the governing equations. In a previous work of Haddad & Corke (1998), the authors adopted the transformation introduced by Davis (1972) in order to remove the singularity at the leading edge in the limiting case when $R = 0$ (i.e. infinitesimally thin flat plate). Since the present study is not concerned with zero thickness bodies, this transformation was not used, instead the above equations were solved directly for ψ and ω for cases where $R > 0$.

2.2. Boundary conditions

First, it should be pointed out that based on (1) and (6), the body surface is located at $\eta_w = R^{1/2}$. Also, since a viscous length scale is used in the current study, the nose radius of curvature, R, becomes Reynolds-number based on the nose radius of curvature, Re, when non-dimensionalized.

2.2.1. *Wall boundary conditions*

At the wall, the no-slip, no-penetration conditions are satisfied by

$$\psi\left(\xi, Re^{1/2}\right) = \text{constant} = 0, \quad \frac{\partial \psi}{\partial \eta}\left(\xi, Re^{1/2}\right) = 0. \tag{9}$$

Also, to generate a condition on the vorticity at the wall, the streamfunction equation (7) is applied at the wall where $\psi_\xi = \psi_{\xi\xi} = \psi_\eta = 0$, giving

$$\omega\left(\xi, Re^{1/2}\right) = \left(\frac{-1}{\xi^2 + \eta^2}\right)\psi_{\eta\eta}. \tag{10}$$

2.2.2. *Free-stream boundary conditions*

The magnitude of the free-stream velocity is set equal to unity since the free-stream velocity is used as a reference velocity scale in (4), that is

$$|U_\infty| = 1. \tag{11}$$

The velocity components of the free stream with a non-zero angle of attack are then

$$u = \cos(\alpha), \quad v = \sin(\alpha), \tag{12}$$

where u and v are the respective velocity components in x-and y-directions, and α is the angle of attack. Recall that the streamfunction is defined as

$$\frac{\partial \psi}{\partial y} = u, \quad \frac{\partial \psi}{\partial x} = -v. \tag{13}$$

The value of the streamfunction in the free stream is therefore defined as

$$\psi_\infty = y\cos(\alpha) - x\sin(\alpha). \tag{14}$$

In parabolic coordinates, the free-stream boundary condition for the streamfunction is then

$$\frac{\partial \psi}{\partial \eta} \to \xi\cos(\alpha) + \eta\sin(\alpha) \quad \text{as} \quad \eta \to \infty. \tag{15}$$

For the vorticity condition, away from the wall, the potential flow has zero vorticity. Therefore

$$\omega \to 0 \quad \text{as} \quad \eta \to \infty. \tag{16}$$

3. Basic flow and perturbation flow equations

A spatial approach is used to formulate the perturbation equations from which we will derive the acoustic receptivity coefficients. The advantage of this approach is that it allows variables with different orders of magnitude to be calculated separately to greater accuracy.

The acoustic wave in the free stream is modelled as a periodic small-amplitude perturbation superposed on the uniform free-stream flow, namely

$$\psi = \psi_\infty + \epsilon e^{i\sigma t}\tilde{\psi}_\infty, \tag{17}$$

where σ is the temporal frequency of oscillation, and ϵ is the amplitude of oscillation, which is sufficiently small for linearization.

Since the mean flow and acoustic wave can be at different incidence angles with respect to the body, as illustrated in figure 1,

$$\psi = (\xi \cos(\alpha) + \eta \sin(\alpha)) + \epsilon e^{i\sigma t}(\xi \cos(\alpha_s) + \eta \sin(\alpha_s)), \tag{18}$$

where α is the angle of attack of the parabolic body with respect to the free-stream streamline, and α_s is the angle of incidence of acoustic (sound) waves with respect to the body centreline. Based on this, we decomposed the unsteady flow field into a steady basic state plus an unsteady perturbation (in normal mode form), given as

$$\psi(\xi, \eta, t) = \Psi(\xi, \eta) + \epsilon e^{i\sigma t}\tilde{\psi}(\xi, \eta), \tag{19}$$

$$\omega(\xi, \eta, t) = \Omega(\xi, \eta) + \epsilon e^{i\sigma t}\tilde{\omega}(\xi, \eta). \tag{20}$$

Substituting these back into the governing equations and boundary conditions, and equating terms of equal powers of ϵ leads to the governing equations for the basic and perturbation flow fields.

The basic flow is governed by the following set of equations (zero-order terms in ϵ)

$$\frac{\partial^2 \Psi}{\partial \xi^2} + \frac{\partial^2 \Psi}{\partial \eta^2} = -(\xi^2 + \eta^2)\Omega, \tag{21}$$

$$\frac{\partial^2 \Omega}{\partial \xi^2} + \frac{\partial^2 \Omega}{\partial \eta^2} + \frac{\partial \Psi}{\partial \xi}\frac{\partial \Omega}{\partial \eta} - \frac{\partial \Psi}{\partial \eta}\frac{\partial \Omega}{\partial \xi} = 0, \tag{22}$$

with the boundary conditions

$$\Psi = 0, \quad \frac{\partial \Psi}{\partial \eta} = 0, \quad \Omega = \left(\frac{-1}{\xi^2 + \eta^2}\right)\frac{\partial^2 \Psi}{\partial \eta^2} \quad \text{at} \quad \eta = Re^{1/2}, \tag{23}$$

$$\frac{\partial \Psi}{\partial \eta} \to \xi \cos(\alpha) + \eta \sin(\alpha), \quad \Omega \to 0 \quad \text{as} \quad \eta \to \infty. \tag{24}$$

The perturbation flow, after linearizing in ϵ, is governed by the following set of equations (first-order terms in ϵ)

$$\frac{\partial^2 \tilde{\psi}}{\partial \xi^2} + \frac{\partial^2 \tilde{\psi}}{\partial \eta^2} = -(\xi^2 + \eta^2)\tilde{\omega}, \tag{25}$$

$$-i\sigma(\xi^2 + \eta^2)\tilde{\omega} + \frac{\partial^2 \tilde{\omega}}{\partial \xi^2} + \frac{\partial^2 \tilde{\omega}}{\partial \eta^2} + \frac{\partial \Psi}{\partial \xi}\frac{\partial \tilde{\omega}}{\partial \eta} + \frac{\partial \Omega}{\partial \eta}\frac{\partial \tilde{\psi}}{\partial \xi} - \frac{\partial \Psi}{\partial \eta}\frac{\partial \tilde{\omega}}{\partial \xi} - \frac{\partial \Omega}{\partial \xi}\frac{\partial \tilde{\psi}}{\partial \eta} = 0, \tag{26}$$

with the boundary conditions

$$\tilde{\psi} = 0, \quad \frac{\partial \tilde{\psi}}{\partial \eta} = 0, \quad \tilde{\omega} = \left(\frac{-1}{\xi^2 + \eta^2}\right)\frac{\partial^2 \tilde{\psi}}{\partial \eta^2} \quad \text{at} \quad \eta = Re^{1/2}, \tag{27}$$

$$\frac{\partial \tilde{\psi}}{\partial \eta} \to \xi \cos(\alpha_s) + \eta \sin(\alpha_s), \quad \tilde{\omega} \to 0 \quad \text{as} \quad \eta \to \infty. \tag{28}$$

By inspecting the above two systems of equations governing the basic flow and the perturbation flow, respectively, we can see that the equations for the basic flow are non-linear, and therefore require an iterative numerical method for their solution. Also, the basic flow equations are real and therefore have a real solution. On the other hand, the equations for the perturbation flow are linear, and therefore can be solved numerically with a direct linear solver. The perturbation equations are,

however, complex, and have a complex solution. Furthermore, the temporal frequency σ appears explicitly in the equations for the perturbation flow, thus the solution is expected to be frequency dependent.

Our interest is in the streamwise variation of the amplitude of the perturbation that couples with the T-S waves of the same frequency. By using this spatial formulation, the basic flow and perturbation flow can be solved separately to the same order of accuracy. This approach allowed us to perform more precise numerical calculations on the perturbation values, and minimize any numerical truncation errors.

4. Grid generation

The contour of the body surface is defined by the line $\eta_w = Re^{1/2}$. The free stream is also defined by the line $\eta = \eta_{max}$. The free stream is set to be at a distance from the wall that is at least ten times the estimated maximum Blasius boundary-layer thickness on a flat plate of the same axial length as the parabolic body and at zero angle of attack. Thus, in the wall normal direction, η varies between the values

$$Re^{1/2} \leqslant \eta \leqslant Re^{1/2} + 35. \tag{29}$$

We used 36 grid points in the computational domain in the η-direction, between the body surface boundary and the free-stream boundary.

On the surface of the body, the leading edge is located at $\xi = 0$. The out-flow boundaries on the lower and upper sides of the body are located at $\xi = -\xi_{max}$ and $\xi = +\xi_{max}$. The out-flow boundary is set far away from the leading edge at $x_{max} = 1.5 \times 10^6$. We have used 2002 grid points in the computational domain in the ξ-direction between $\xi = -\xi_{max}$ and $\xi = +\xi_{max}$. This guaranteed a minimum of 10 points per T-S wavelength.

In order to capture the physical phenomenon more accurately, more grid points were located near the wall in the η-direction, and near the leading edge in the ξ-direction. This was done using Robert's stretching transformation of the original uniform grid (Anderson, Tannehill & Pletcher). The transformation used is given by

$$\hat{y} = h\frac{(\beta+1) - (\beta-1)[(\beta+1)/(\beta-1)]^{1-\bar{y}}}{[(\beta+1)/(\beta-1)]^{1-\bar{y}} + 1}, \tag{30}$$

where, in general, $\bar{y}$ represents the original uniformly spaced grid points and $\hat{y}$ are the stretched grid points and β is the stretching parameter. In the present study, $\beta = 1.25$ in the ξ-direction, and $\beta = 1.005$ in the η-direction since these values provided sufficiently smooth and accurate results.

The geometry we are dealing with is a semi-infinite body. Since the numerical calculations cover a finite domain, the buffer domain technique used by Haddad & Corke (1998) and Erturk & Corke (2001) was used to provide the outflow boundary condition. The approach is to gradually kill the elliptic ($\partial^2/\partial\xi^2$) terms in the governing equations in a buffer zone at the downstream end of the computational domain. To accomplish this, these elliptic terms were multiplied by a weighting factor $\hat{s}$. At the beginning of the buffer zone, $\hat{s} = 1$. At the end of the buffer zone, $\hat{s} = 0$. In between, $\hat{s}$ changes according to

$$\hat{s}(i) = \frac{\tanh(4) + \tanh(arg)}{2\tanh(4)}, \tag{31}$$

where

$$arg = 4\left(1 - \frac{2(i - ibuf)}{(imax - ibuf)}\right), \tag{32}$$

and i is the numerical streamwise index, *imax* is the numerical index of the last grid point in the streamwise direction, and *ibuf* is the index (i) of the first grid point at the beginning of the buffer zone. The length of the buffer zone used in this study was equivalent to approximately five T-S wavelengths, which was well beyond the recommended minimum of three used in the previous study by Haddad & Corke (1998).

5. Numerical method

For the solution of the nonlinear steady basic flow equations, we developed an iterative numerical method. The basic flow variables are improved through a pseudo-time marching until convergence is achieved. More details on the numerical method can be found in Erturk (1999). For the solution of the linear perturbation equations, we used an efficient direct linear solver (LINPACK subroutines). The solution methodology of the problem is to first solve the basic flow equations for a given angle of incidence, α. Using the basic flow solution, the coefficients in the perturbation equations were next calculated. With specified values of the frequency, σ, and angle of incidence of the acoustic waves, α_s, the perturbation equations are then solved.

In the results presented here, the angle of incidence of the acoustic waves, α_s, was always equal to that of the body, α. Erturk & Corke (2001) have examined the effect of different angles of incidence of sound waves ($\alpha_s \neq \alpha$) on the non-aerodynamically loaded ($\alpha = 0$) parabolic body.

For the numerical solution of the perturbation equations, we used the same numerical grid and buffer zone that was used for the solution of the basic flow equations. We note that all of the results presented here are grid independent.

6. Results and discussion

Extensive numerical tests have been carried out to study the effect of the numerical grid size, and outflow and free-stream boundary locations. In particular, we focused on the mean flow, where the use of the parabolic body at zero angle of attack has the advantage that the mean flow becomes Blasius downstream of the leading edge. Comparisons between the mean wall shear stress and vorticity in a related study (Erturk, Haddad & Corke 2004), provided a check on the accuracy of the solutions for the range of nose radii used here. The results of these numerical checks are identical to those previously presented by Haddad & Corke (1998) and Erturk & Corke (2001).

6.1. *Sample mean flow results*

Three nose Reynolds numbers of 10, 50 and 100 were examined. The mean flow for a range of angles of incidence was computed. The angles ranged from zero, to a value that was beyond where the flow would separate. This separation angle increased as the nose Reynolds number increased. The range of angles, and the angle where the flow first separates are summarized in table 1.

The overall effect of angle of incidence on the mean flow over the parabolic body is best shown through the velocity streamlines. These are presented in figure 2 for $Re = 10$ at four different angles of 0°, 6°, 13° and 14°. At 0°, the stagnation streamline perfectly aligns with the body centreline axis. At the next higher angle of incidence

Re	α range (deg.)	α_{sep}
10	0–14	12
50	0–18	$\simeq 17$
100	0–21	$\simeq 20$

TABLE 1. Nose Reynolds numbers and angles of incidence examined.

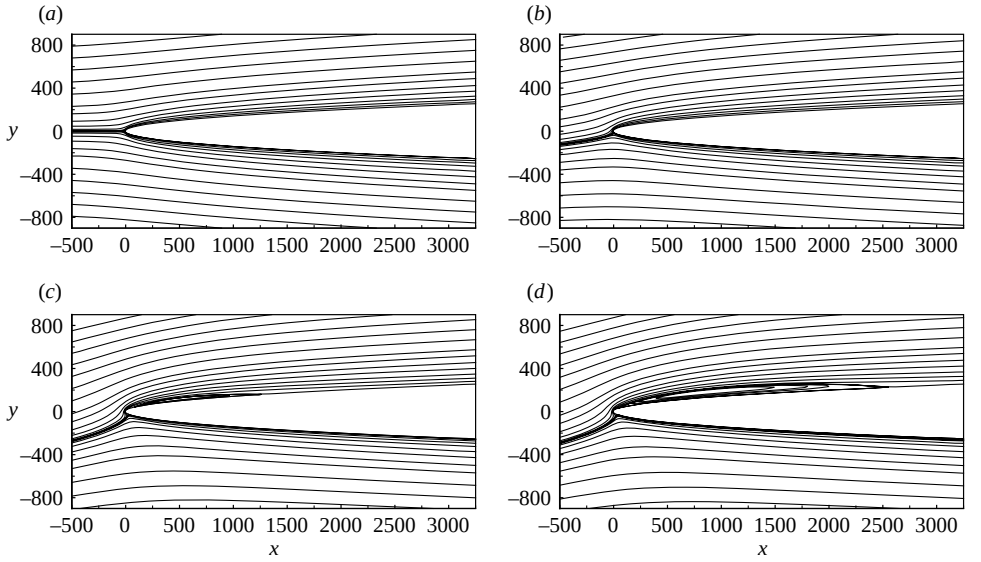

FIGURE 2. Velocity streamlines for the flow over the parabolic body at four different angles of incidence for $Re = 10$. (*a*) $\alpha = 0°$, (*b*) 6°, (*c*) 13°, (*d*) 14°.

presented in the figure, 6°, the stagnation streamline is curved and impacts the body below the physical leading edge. As will be shown, this results in a strong pressure gradient at the leading edge.

At this Reynolds number, the mean flow first separates at an angle of 12°. The separation 'bubble' is evident in the streamline pattern near the body surface at the higher angles of incidence of 13° and 14° shown in figure 2. The effect that the separation 'bubble' has on the acoustic receptivity and growth of the T-S instability downstream is a primary focus of this work.

A quantitative measure of the locations of the mean flow separation and reattachment comes from viewing the streamwise distribution of the surface friction coefficient, $C_f = \tau_w^*/\rho U_\infty^2$, where $\tau_w^* = \mu(\partial u^*/\partial y^*)|_w$. These are shown in figure 3 for the three nose Reynolds numbers over the full range of angles of incidence of the body. The value $C_f = 0$ is shown as the horizontal dotted line. At any nose Reynolds number, the upstream location where C_f crosses through zero to become negative, marks the separation location. The next downstream position where C_f crosses zero to become positive, indicates where the mean flow reattaches.

Focusing on $Re = 10$ in figure 3, the flow first separates at 12°. This occurs at $\xi = 20$. The length of the separation bubble at this angle is fairly small, extending to approximately $\xi = 30$. As the angle of attack increases, the separation point moves further upstream, closer to the leading edge, and the length of the separation zone

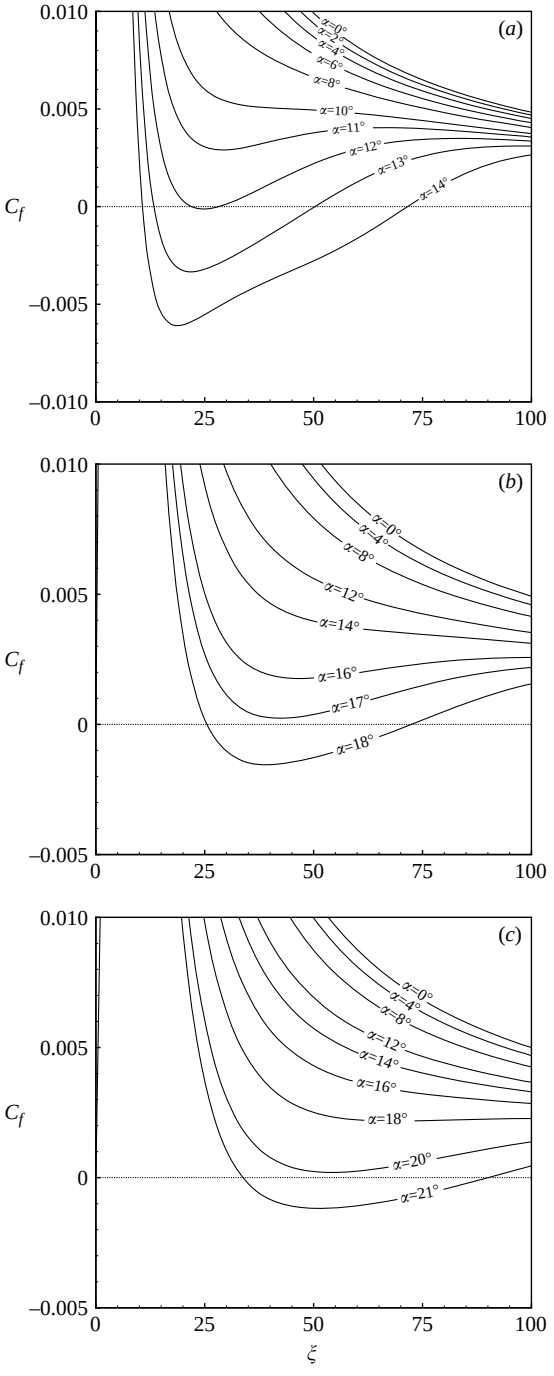

FIGURE 3. Surface friction coefficient distributions along parabolic body for different angles of attack at (*a*) $Re = 10$, (*b*) 50 and (*c*) 100.

increases almost linearly with angle of attack. At $Re = 50$, the separation bubble first forms a little beyond an angle of incidence of 17°. At $Re = 100$, the separation angle increases to just past 20°.

In all these cases, the location and extent of the separation bubble is relatively close to the leading edge, although it never extends to the leading edge ($\xi = 0$). As a reference, it corresponds to less than 1.5 % of the computational domain. More importantly for our objective, it is far upstream of the linear stability Branch I, and the length of the separation bubble corresponds to a fraction of a T-S wavelength at the frequency of interest.

6.2. *Perturbation flow results*

These results deal with the solution of the perturbation flow that is governed by (25) to (28). With this we are examining the response of the unsteady flow to an infinitesimal (linear) periodic disturbance that is superimposed on the uniform mean flow as given by (17). We non-dimensionalize the disturbance frequency such that σ is defined as

$$\sigma = \frac{2\pi f \nu}{U_\infty^2}. \tag{33}$$

The results that follow are for $\sigma = 230 \times 10^{-6}$. This was chosen to match the conditions in the computations of Haddad & Corke (1998). This frequency crosses the upper tip of the neutral curve for the linear growth of disturbances in the boundary layer. Besides allowing a comparison to the earlier work, the choice of this frequency offers some other advantages. The first is that at this frequency, the amplification distance is relatively short so that we could easily reach the location of the second neutral branch (II) within our computational domain. This allows us to determine the Branch II receptivity coefficient which will combine the effects of both the leading edge and separation bubble on the downstream instability growth. Secondly, this frequency is far from the most amplified value so that we are less likely to violate the linear assumptions in the anticipated high-instability amplitude levels that will occur with the separation bubble present. For a physical reference to experiments, for example in air, with $\nu = 1.5 \times 10^{-5}\,\mathrm{m^2\,s^{-1}}$ and a free-stream velocity $U_\infty = 6.7\,\mathrm{m\,s^{-1}}$, the dimensional frequency is 109.53 Hz.

In terms of the boundary-layer instability, the most appropriate Reynolds number is based on the surface arclength along the parabolic body, $s(x)$, where

$$s(x) = \tfrac{1}{2}R\left\{\left(1+\frac{2x}{R}\right)^{1/2}\left(2+\frac{2x}{R}\right)^{1/2} + \ln\left[\left(1+\frac{2x}{R}\right)^{1/2} + \left(2+\frac{2x}{R}\right)^{1/2}\right]\right\}. \tag{34}$$

Since a viscous length scale is used in our non-dimensionalization, s and Re_s are identical.

An example of the type of result we obtain for the perturbation flow is shown in figure 4. This is for $Re = 10$ and $\alpha = 0$. It corresponds to the streamwise perturbation velocity (u) with respect to the Reynolds number (Re_s) along the body, at a fixed height above the surface that is close to where the amplitude is a maximum. The u-axis has been magnified in order to see the instability waves, in the linear amplified region ($7 \leqslant Re_s \times 10^4 \leqslant 14$). With this, the spatial oscillations are clearly evident although further analysis is needed to isolate the component of the fluctuations that is explicitly due to T-S waves.

In presenting the perturbation flow, the contribution of the Stokes wave is always subtracted from the total perturbation velocity. This involves an independent solution of the governing equations that have been modified to eliminate the inertia terms. The equations for the Stokes flow are discretized on the same numerical grid used for the other calculations. The Stokes flow solution is then subtracted point by point

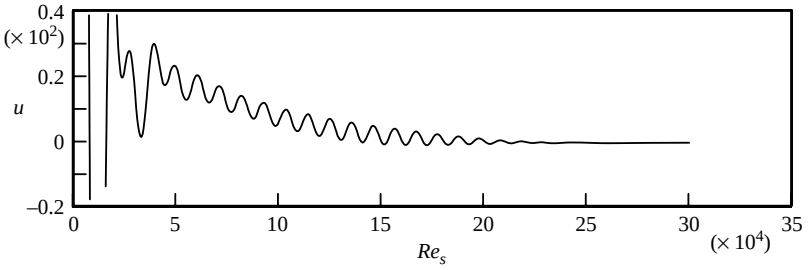

FIGURE 4. Sample streamwise perturbation velocity (u) along the body at a fixed height that is close to the amplitude maximum; $Re = 10$, $\alpha = 0°$.

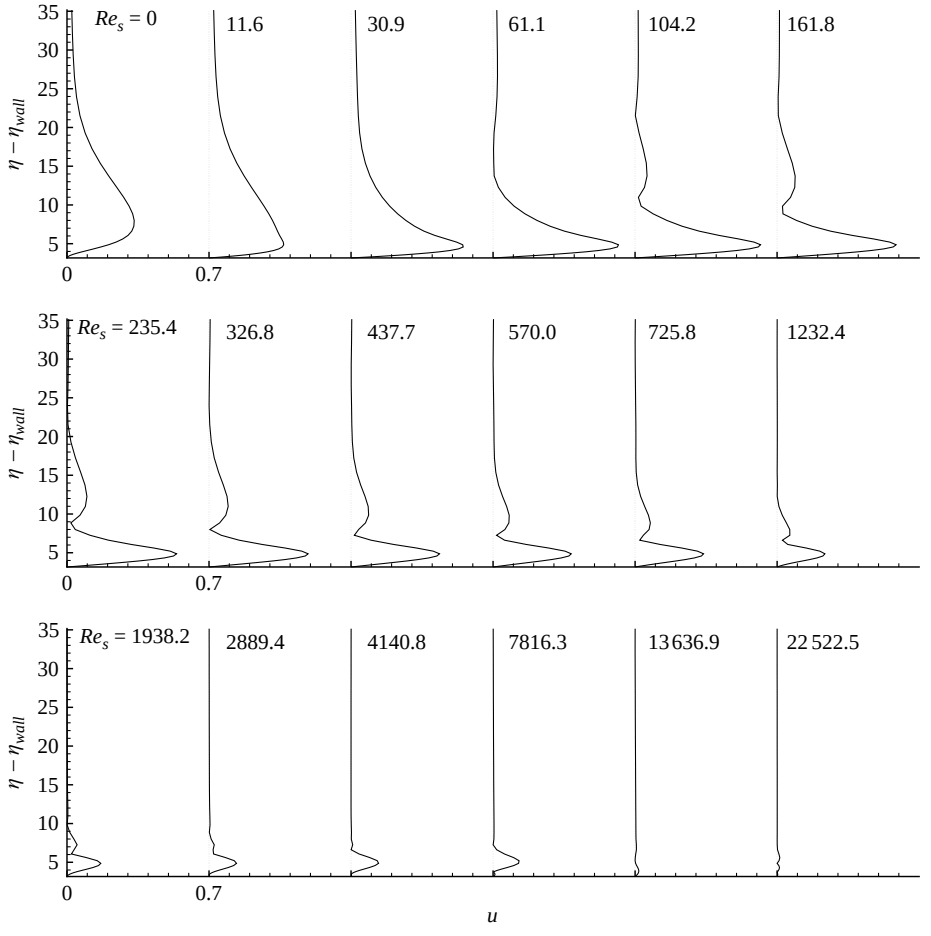

FIGURE 5. Streamwise (u) perturbation velocity profiles at consecutive downstream locations with Stokes wave removed; $Re = 10$, $\alpha = 0°$.

from the total perturbation solution. An example of this process can be found in the papers by both Haddad & Corke (1998) and Erturk & Corke (2001).

Figure 5 shows wall-normal distributions of the streamwise (u) perturbation velocity (after subtracting the Stokes flow) at consecutive streamwise positions, starting at the leading edge, for $Re = 10$ and $\alpha = 0°$. We note that at the first four positions shown,

the wall-normal distributions do not resemble a T-S eigenfunction. Near the leading edge, we suspect the perturbation flow, after subtracting off the Stokes wave, is made up of a combination of forced (non-Orr–Sommerfeld) modes and T-S modes. Further downstream of the leading edge, for example at $Re_s = 104.2$, the wall-normal streamwise velocity profiles eventually develop a T-S eigenfunction shape. Based on the lower peak in the wall-normal profile, we observe the amplitude to decrease with downstream distance. This is expected since all of the locations shown in figure 5 are well upstream of Branch I, which occurs at $Re_s \approx 7.0 \times 10^4$.

6.2.1. *Leading-edge receptivity*

Our interest here is in the leading-edge receptivity coefficient for the T-S waves. In general, we define the receptivity coefficient at any s-location, as the ratio of the maximum T-S amplitude to that of the free-stream disturbance, namely $K_s = |u_{TS}|/|u_\infty|$. In our formulation, the perturbation amplitude obtained from the numerical results is u/u_∞. Therefore, if the only component of the fluctuations is due to T-S waves, the amplitude we measure at any s location, such as the profiles in figure 5, are identical to K_s.

Therefore, the remaining step in obtaining the leading-edge receptivity coefficient is to extrapolate the value corresponding to T-S waves upstream to the leading edge. To achieve this, we select the maximum values in the wall normal profiles that have a T-S eigenfunction shape near the leading edge. An exponential fit is then performed which is then used to extrapolate to the leading-edge value to determine K_{LE}.

An example of the exponential fit and leading-edge extrapolation is shown in figure 6 for $Re = 10$ at $\alpha = 0°$ and 6°. This is plotted on log–linear axes to illustrate better the exponential decay in u with Re_s. In both cases, we easily identify an exponential decay region near the leading edge. When we extrapolate these fits to the leading edge ($\xi = 0$) we note that K_{LE} increased with angle of attack.

The process of determining K_{LE} was performed for the three leading-edge Reynolds numbers at all of the angles of attack, up to where separation occurred. The result is shown in figure 7. In general, the leading-edge receptivity coefficient increases with angle of incidence in an approximate linear fashion. In addition, the overall magnitude and change with angle is largest for the smaller nose radius. The increasing K_{LE} with decreasing nose radius agrees with the past results of Haddad & Corke (1998) for zero angle of incidence.

Hammerton & Kerschen (1992) suggest that the appropriate way to normalize the angle of incidence in the abscissa in figure 7 is by the square-root of the nose radius (Reynolds number in dimensionless form). The result is shown in figure 8. In this we observe some degree of collapse of the three sets of results, however, there still appears to be a systematic difference between the three leading-edge radii at the smaller angles of incidence.

Overall, the trend of increasing K_{LE} with angle of incidence is consistent with the asymptotic results of Hammerton & Kerschen (1992). However, they had observed that with small aerodynamic loading (angles of incidence) there was an initial slight decrease in the leading-edge receptivity. Our present results, and those of Haddad & Corke (1998) have not observed this decrease in K_{LE} at small angles.

What is the physical explanation for the increase in the K_{LE} with increased aerodynamic loading? Could it possibly be due to the movement of the adverse pressure gradient region towards the region of receptivity (leading edge)? Although this does happen, the pressure gradient near the leading edge for the parabolic body

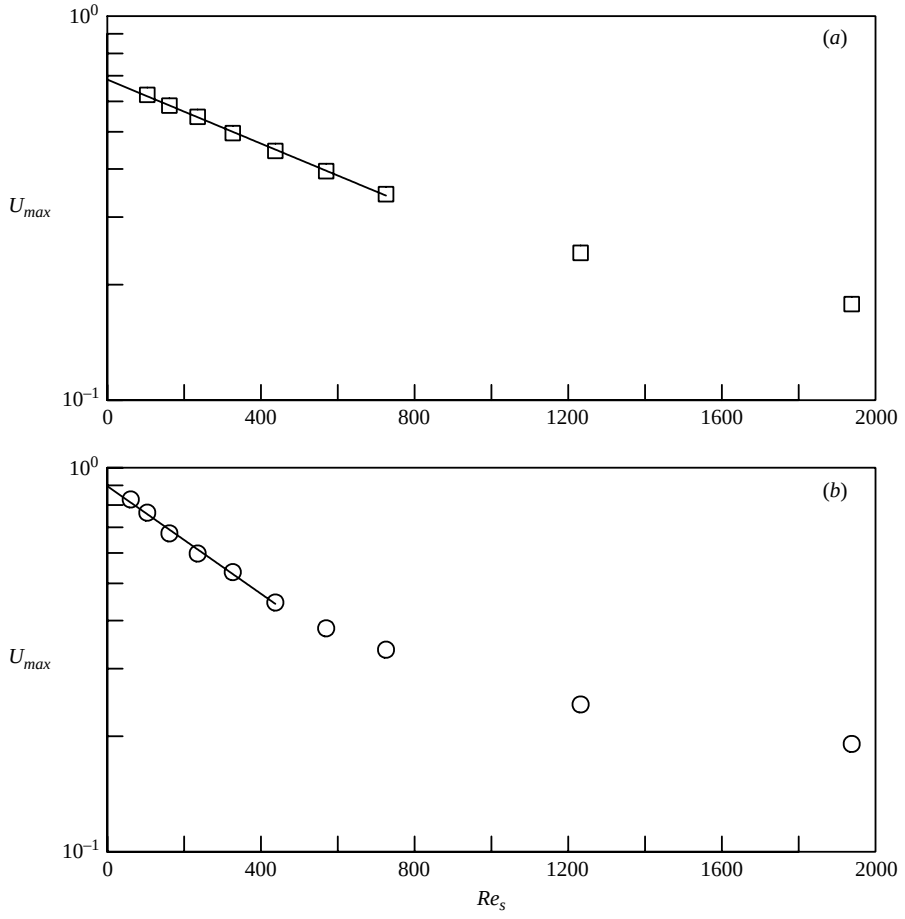

FIGURE 6. Example of the extrapolated leading-edge receptivity coefficient value found by fitting spatial exponential decay of peak u fluctuations; $Re = 10$, (a) $\alpha = 0^\circ$ and (b) $\alpha = 6^\circ$.

for the angles up to flow separation, never became adverse. An example of the pressure gradient, $\partial P/\partial \xi$, distribution for the body at $\alpha = 4^\circ$ and $Re = 10$, is shown in figure 9(a). At zero angle of incidence, the stagnation line is at the leading edge ($\xi = 0$) and $\partial P/\partial \xi = 0$. With $\alpha > 0$, the stagnation point moves to the lower surface (negative ξ), below the leading edge (see figure 2), and a pressure gradient develops at the leading edge. This gradient is favourable. As the angle of incidence increases, the pressure gradient at the leading edge continues to increase. This is documented in figure 9(b). The increase in the pressure gradient at the leading edge continues until the flow separates, which is at $\alpha = 12^\circ$ for $Re = 10$.

We view the local pressure gradient at the leading edge as an amplifier in the wavelength conversion of the free-stream acoustic disturbances. As the gradient increases, we expect a larger response to free-stream fluctuations, which is manifest as the increase in K_{LE} with angle of incidence in figure 7. We note that in the range of angles in figure 7 for $Re = 10$, K_{LE} increases approximately linearly, as does $\partial P/\partial \xi$.

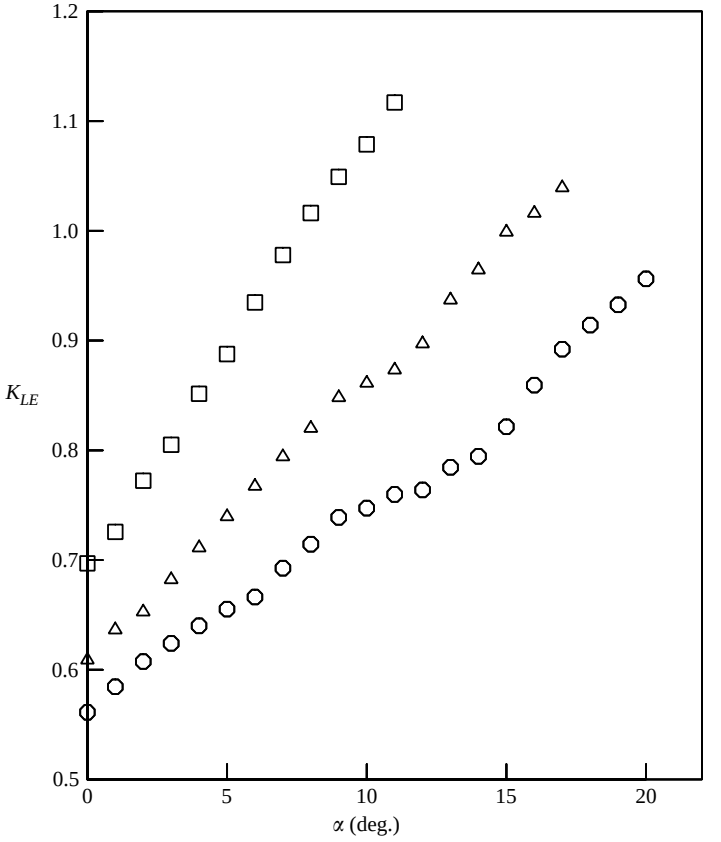

FIGURE 7. Leading-edge receptivity coefficients for □, $Re = 10$, △, 50 and ○, 100 as a function of the parabolic body angle of attack prior to flow separation.

6.2.2. *Branch-II receptivity*

One of our principle interests is on the effect of the flow separation, that occurs at large angles of incidence, on the growth of the T-S waves. Our expectation is that the separation bubble will provide another receptivity site, similar to the leading edge.

Because the separation bubble is always downstream of the leading edge in our cases, to observe its effect, we focus on the maximum T-S wave amplitude downstream, at Branch II. For this, we define a Branch II receptivity coefficient, $K_{II} = |u_{TS}|_{II}/|u_\infty|$. The Branch II receptivity coefficient is the most convenient quantity to relate to experiments because the larger amplitudes make it easier and more accurate to measure. K_{II} can of course be related to the leading-edge receptivity by determining the equivalent Branch I amplitude based on linear-theory growth, and extending from that point to the leading edge through an appropriate theory or N-S calculations for the leading-edge flow.

One of the difficulties in determining $|u_{TS}|_{II}$ at our disturbance frequency is that the T-S amplification rate is small. As a result of this, Haddad & Corke (1998) observed that in the linear amplified region, the amplitude of the discrete T-S mode was comparable to those of the continuous spectrum of Orr–Sommerfeld modes. The effect of this was observable as a modulation in the spatial amplitude of the discrete T-S wave. An example can be seen in the amplitude distribution shown in figure 4.

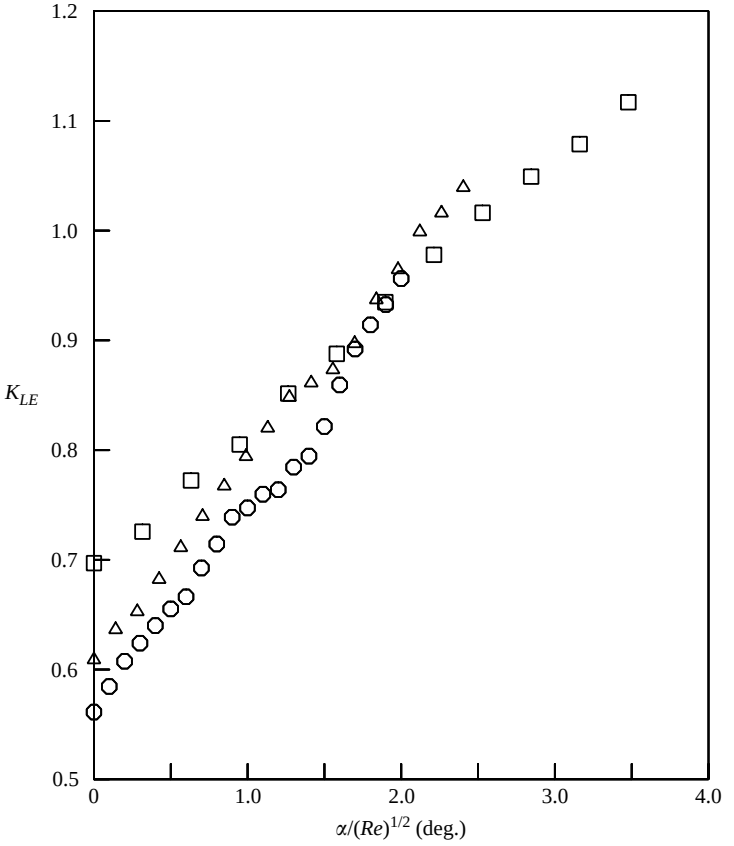

FIGURE 8. Leading-edge receptivity coefficients for □, $Re = 10$, △, 50 and ○, 100 as a function of the parabolic body angle of attack normalized by the leading-edge Reynolds number.

In particular, it is most evident around $Re_s \simeq 5 \times 10^4$. Similar modulations have also been observed by Murdock (1980), Buter & Reed (1994), and Gatski & Grosch (1987). The presence of these modes makes it more difficult to determine the true discrete T-S amplitude distribution.

In order to separate out the contribution of the discrete T-S fluctuations from the total u-perturbation distributions, such as in figure 4, we followed the approach previously used by Haddad & Corke (1998). This involved applying a one-dimensional spatial high-pass filter that was designed to reject fluctuations with wavelengths larger than the expected discrete T-S wavelength. The assumption in doing this was that the wavelength of the continuous spectrum modes are two to three times larger than those of the discrete T-S modes. The high-pass filter cut-off was therefore designed to suppress energy at wavelengths that were greater than or equal to twice the expected discrete T-S wavelength. The filter was convolved with the spatial perturbation distribution. A sample result is presented in figure 10, which compares the original u-distribution (figure 10*a*), to that of the filtered distribution (figure 10*b*). Following the filtering to remove the contribution of the continuous spectrum modes, the amplified region between Branch I ($Re_s \simeq 70\,000$) and Branch II ($Re_s \simeq 140\,000$) of the discrete T-S mode is then clearly visible.

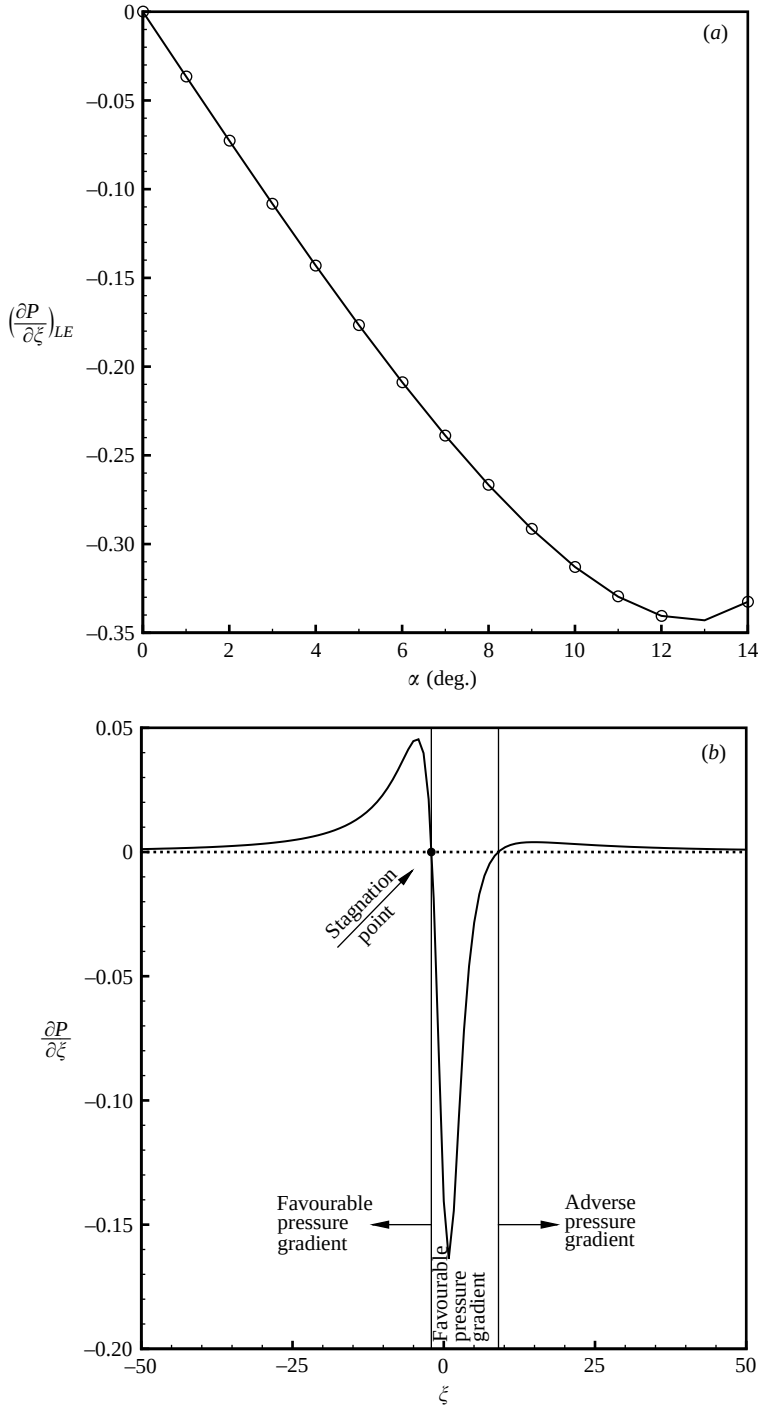

FIGURE 9. (*a*) Pressure gradient distribution around body at $\alpha = 4^\circ$ and (*b*) pressure gradient at leading edge ($\xi = 0$) versus angle of incidence of body; $Re = 10$.

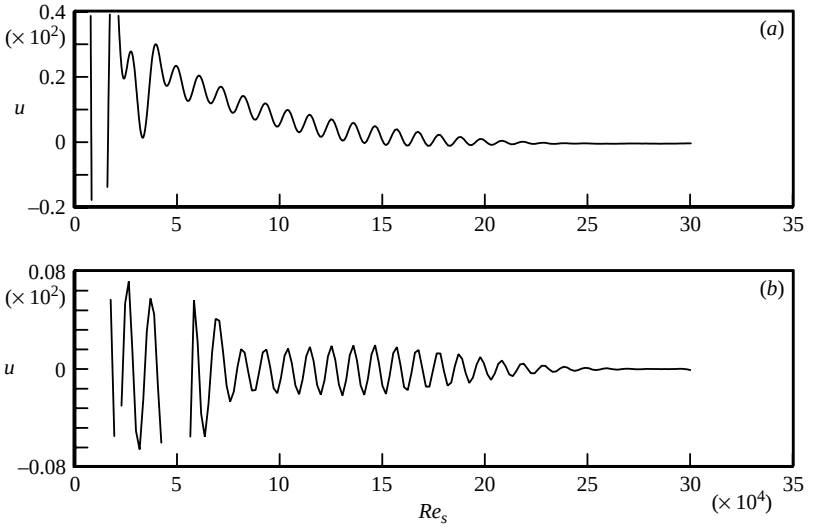

FIGURE 10. Sample streamwise perturbation velocity (u) along the body at a fixed height that is close to the amplitude maximum (a) before and (b) after applying high-pass filter to remove contributions of continuous spectrum modes; $Re = 10$, $\alpha = 0°$.

In order to check further that the mode that remains after filtering is the discrete T-S mode, we filtered the u-perturbation distributions at all of the computed heights above the surface of the parabolic body, and measured the maximum u amplitude at Branch II. These are plotted in figure 11 for $Re = 10$ and $\alpha = 0°$. For reference, we have also plotted as a solid curve, the T-S eigenfunction from a linear stability calculation at our frequency and Re_s location. Overall, the comparison between the computed amplitudes and linear theory is very good.

We obtain an initial sense of the effect the angle of incidence has on the T-S mode growth in the amplified region in figure 12. This shows the filtered u-perturbation distributions at the height where the amplitude is the maximum, at increasing angles of incidence from 0° to 14° for $Re = 10$. The scale on u is the same on all of the plots in the figure except for having different orders of 10 multipliers. For example, at $\alpha = 0°$ the multiplier is 10^3, whereas at $\alpha = 14°$ the multiplier is 10^0. From this it is evident that the amplitude of the T-S wave is approximately 1000 times larger at $\alpha = 14°$ than at $\alpha = 0°$. It is also evident in figure 12 that there was a disproportionate growth in the T-S amplitude between $\alpha = 12°$ and 14°. The significance of this is that the separation bubble first forms at $\alpha = 12°$.

The maximum u-amplitudes at Branch II have been compiled for all three leading-edge Reynolds numbers, at all of the angles of incidence. These are presented in terms of the Branch II receptivity coefficient, K_{II} in figure 13. Because of the large dynamic range of K_{II} in these cases, it is presented on a log axis. The angle of incidence has not been normalized by Re as was done in figure 8, because the differences due to the nose Reynolds numbers observed at smaller angles are fairly insignificant compared to the effects at large angles.

If we first focus on the results in figure 13 for the largest leading-edge Reynolds number (100), we observe a smooth increase in K_{II} with increasing α. In this case, the flow first separates at $\alpha \simeq 21°$, which is the last point in the set.

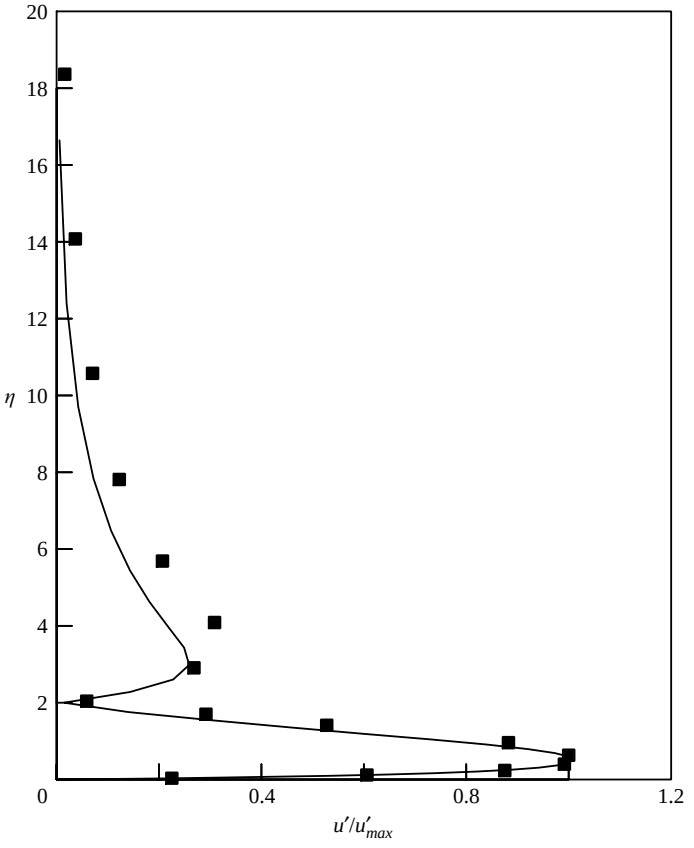

FIGURE 11. Wall-normal amplitude profile at the location of Branch II after high-pass filtering to remove long-wavelength fluctuations (square symbols), and comparison to linear theory discrete T-S eigenfunction (curve); $Re = 10$, $\alpha = 0°$.

The values for the next smallest Reynolds number (50) lie on top of those at $Re = 100$ for angles up to approximately 15°. Above this angle, the K_{II} values are larger than those for $Re = 100$, at the same angles. For $Re = 50$, the flow first separates at $\alpha \simeq 17°$. Therefore, the more rapid increase in K_{II} compared to $Re = 100$ appears to precede this by about 2°.

Finally at the lowest Reynolds number (10), at the smaller angles to approximately $\alpha = 5°$, the values of K_{II} closely overlies those of the other two Reynolds numbers. The separation bubble in this case forms at $\alpha \geqslant 12°$. There appears to be a small levelling out of the K_{II} values up to $\alpha = 10°$, which is then followed by a very rapid increase in K_{II} that again precedes the mean flow separation angle by approximately 2°.

In order to try to explain the behaviour of K_{II} with changing angle of incidence, we will focus on the $Re = 10$ case. Prior to any flow separation, the only site of receptivity to acoustic free-stream disturbances on the body is the leading-edge. The growth of the T-S waves in the amplified region downstream that is reflected in K_{II}, takes its seed from the leading-edge receptivity.

Focusing then on K_{LE} for $Re = 10$ in figure 7, we observe an almost linear increase with angle of incidence to approximately $\alpha = 6°$. Above this angle, the increase in the

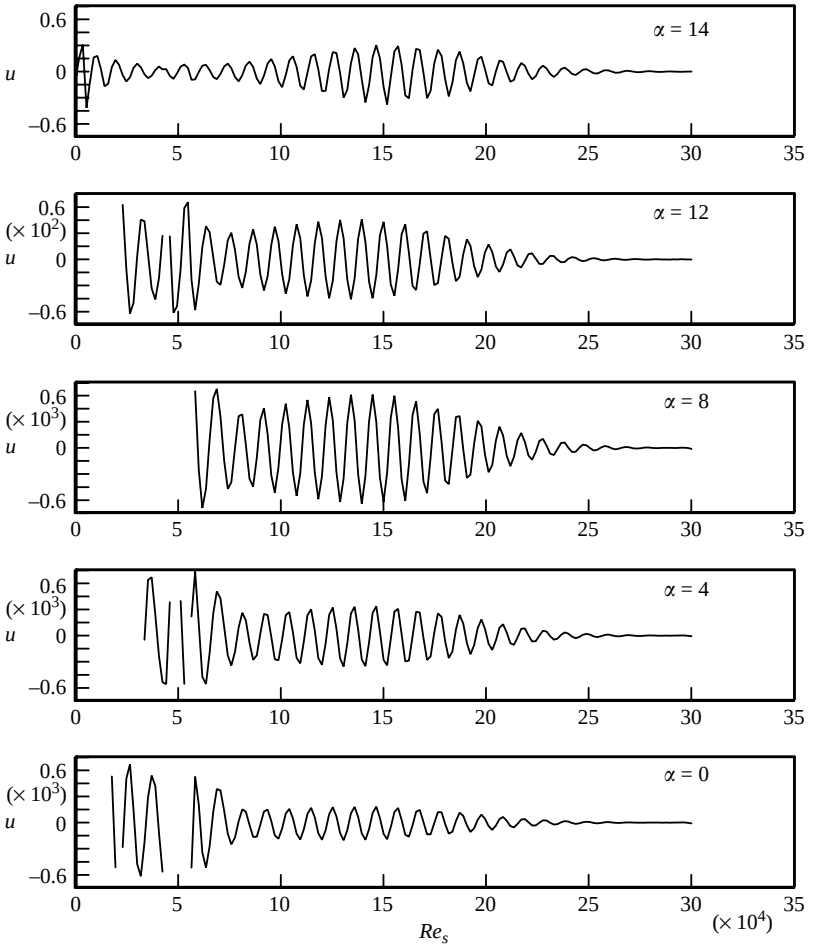

FIGURE 12. Filtered streamwise perturbation velocity (u) along the body at a fixed height that is close to the amplitude maximum at different angles of incidence; $Re = 10$. Note scale multiplier is changing to accomodate increasing amplitudes with increasing α.

leading-edge receptivity coefficient with increasing angle decreases. This behaviour correlates with the pressure gradient, $\partial P/\partial \xi$ at the leading edge, that was shown in of figure 9(b). There, the gradient increases almost linearly up to approximately $\alpha = 6^\circ$, and then changes less until it saturates at $\alpha \geqslant 12^\circ$ where the flow first separates. As pointed out earlier, we believe the increase in $(\partial P/\partial \xi)_{LE}$ is directly linked to the increase in K_{LE} with increasing angle of incidence.

The smaller increase of K_{LE} with angles of incidence between 7° and 10° can therefore explain the small plateau in the K_{II} values in the same range of angles that was documented in figure 13. What explains the more rapid increase in K_{II} at angles above these?

The singular event in the mean flow over the body at the higher angles of incidence $\geqslant 12^\circ$, is the formation of the separation bubble. Table 2 summarizes the locations of the separation and reattachment points for $Re = 10$, as well as the length of the separation bubble as a percentage of the T-S wavelength. Also included in table 2 are

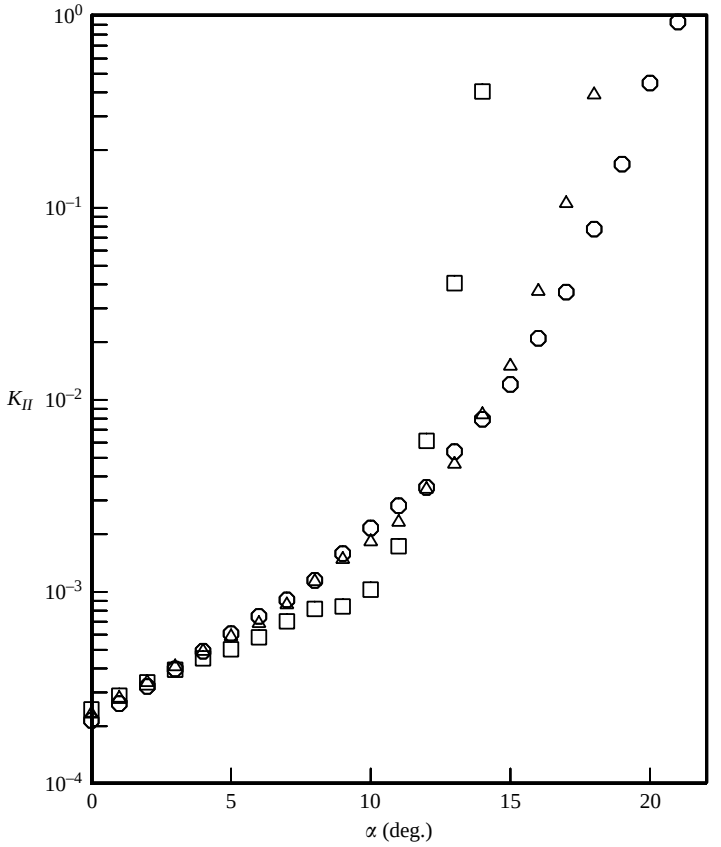

FIGURE 13. Branch II receptivity coefficients for $Re = \square$, 10, $\triangle$, 50 and $\bigcirc$, 100 as a function of the parabolic body angle of incidence.

α (deg.)	$(Re_s)_{sep}$	$(Re_s)_{ret}$	$\%\lambda_{TS}$	$(Re_s)_I$	$(Re_s)_{II}$
12	252	425	4.3	65,091	139,372
13	99	1305	13.1	63,350	137,882
14	68	2595	26.0	52,146	146,530

TABLE 2. Separation characteristics for $Re = 10$.

the locations of Branches I and II based on streamwise distributions of the filtered u-perturbations such as shown in figure 12.

At smaller angles of incidence, below which the mean flow separated, the disturbances in the boundary layer decayed exponentially from the leading edge until they reached the Branch I location. Examples of this were shown in figure 6, and were the basis of the exponential fit and extrapolation used to determine K_{LE}. This behaviour is however different when the flow separates. To show this, we focus on $\alpha = 14^\circ$ which has the largest separated region.

Figure 14 shows the streamwise development of the maximum u-perturbation taken from wall-normal distributions like those in figure 5, but at $\alpha = 14^\circ$. This maximum is indicative of the lower peak in the wall-normal T-S eigenfunction, and is therefore a

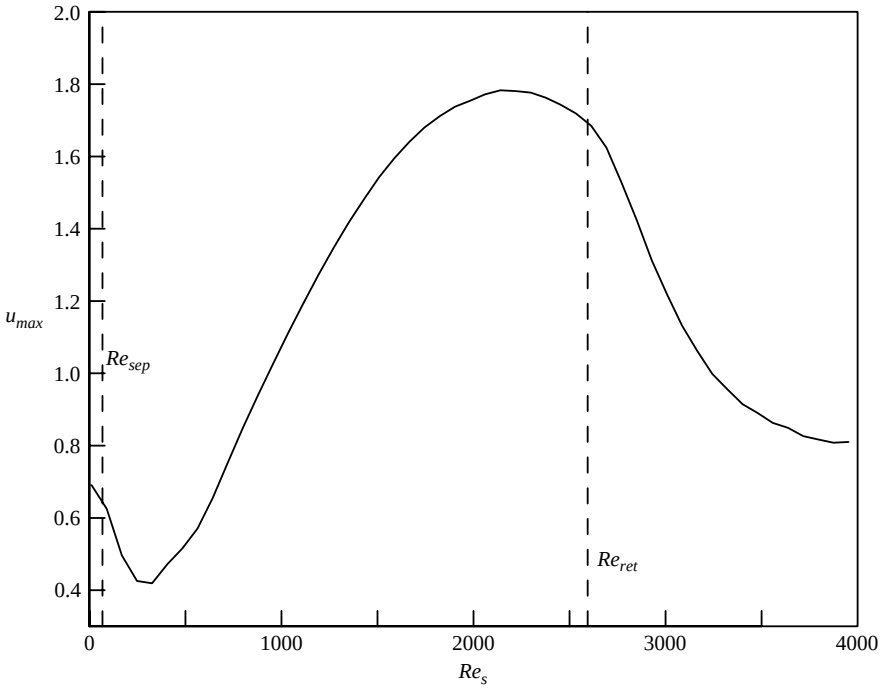

FIGURE 14. Maximum streamwise perturbation amplitude along body $Re = 10$ and $\alpha = 14°$. Dashed lines mark locations of mean flow separation and reattachment.

measure of the T-S wave amplitude. The two vertical dashed lines in figure 14 denote the locations of the separation and reattachment points on the body.

As with the lower angle of incidence cases, the maximum u value decreases downstream of the leading edge with $\alpha = 14°$. This continues a short distance into the separated zone, but in contrast with the lower angle cases, the maximum u value grows to more than twice the leading-edge value by the end of the separation region. Recall that in our formulation the perturbation amplitude obtained from the numerical results is u/u_∞. Therefore the amplitude we measure at any s location, is identical to the receptivity coefficient, K_s. Thus based on this, the receptivity coefficient for the separation bubble in this case is 1.77, which is more than twice that of K_{LE} at this angle (which is less than at the highest angle before separation), and approximately 60 % larger than the largest K_{LE}, that occurred just prior to separation (see figure 7). Note that this increase in amplitude occurs in a streamwise distance that is only approximately 4 % of the TS wavelength (see table 2). This would suggest that it is more representative of a receptivity site than a region of enhanced linear growth.

Past the reattachment point, the T-S amplitude again decreases exponentially until the Branch I location is reached. However, the combination of a lack of exponential decay in the separation zone, and the added growth of the T-S wave amplitude, leads to two orders of magnitude larger T-S amplitudes by the Branch II location compared to the conditions before separation. The differences in K_{II} for $\alpha = 12°$ to $14°$ reflects the extent of the separation zone, which increases approximately linearly with increasing angle of incidence in this range of angles.

Thus when the mean flow separates on this body, there become two sites of receptivity: at the leading edge, and at the location of the separation zone.

Originally, we thought there could be the potential for an interaction (through linear superposition) of waves originating at these two sites, that was similar to that documented by Wanderley & Corke (2001) on the elliptic leading edge of a flat plate. If this were to occur, we would expect to find a frequency selection mechanism in which the waves originating from the two sites would linearly add or subtract based on the number of T-S wavelengths between the two sites. However as table 2 indicates, the distances between the leading edge and the separation zone are only a fraction of a T-S wavelength, with the largest being only approximately $\lambda/4$. In addition, our dimensionless frequency ($\sigma = 230 \times 10^{-6}$) is at the very top of the neutral curve, and more amplified frequencies will have longer wavelengths making the percentage even smaller. Therefore aside from differences in the linear amplification rates of the T-S mode, we do not expect behaviour that is different from what was presented here for other disturbance frequencies.

7. Conclusions

The spatial formulation used in this problem was successful in capturing the mean flow separation at large angles of incidence, and its effect on the growth of discrete T-S waves at the linear stability Branch II. For angles of attack before separation, we found that the leading-edge receptivity coefficient, K_{LE}, increased with angle of incidence. The magnitude and change with angle of incidence increased as the leading-edge radius decreased. This followed an increase in the pressure gradient at the physical leading edge as the angle of attack increased. The magnitude of the pressure gradient decreased with increasing leading-edge radius, which correlates with the lower K_{LE} in those cases. Normalizing the angle of incidence by the square-root of the leading-edge Reynolds number gave a moderate amount of collapse of K_{LE} versus α for the range of conditions examined. At larger angles of incidence, a separation zone formed that became a second site of receptivity to the free-stream disturbance. For the smallest leading-edge radius examined corresponding to $Re = 10$, and an angle that was 2° past where the flow first separated, the receptivity coefficient of the separation zone was more than twice that of the leading edge. This led to a T-S amplitude more than 100 times larger at the Branch II location (K_{II}). The receptivity coefficient of the separation zone increased with its streamwise extent, which increased approximately linearly with angle of attack. The scenarios for the other larger leading-edge (radii) Reynolds numbers are similar after accounting for their respective leading-edge receptivity and location and extent of the separation zone. Even with the largest Reynolds number, with the lowest K_{LE}, the Branch II amplitude of T-S waves at the angle where the flow first separated was almost four orders of magnitude larger than those at zero angle of incidence. This emphasizes the importance that aerodynamic loading and flow separation have on acoustic receptivity, and therby on boundary-layer transition to turbulence.

O. H. is grateful for Jordan University of Science & Technology (JUST) for granting him a sabbatical leave to participate in this work. He is also grateful for the financial support provided by the University of Notre Dame Center for Flow Physics and Control (FlowPAC).

REFERENCES

Anderson, D. A., Tannehill, J. C. & Pletcher, R. H. 1984 *Computational Fluid Mechanics and Heat Transfer*. McGraw-Hill, New York.

Asai, M. & Kaneko, M. 2000 Experimental investigation of receptivity of a shear layer separating at a convex corner. *Fluid Dyn. Res.* **27**, 117–128.

Buter, T. A. & Reed, H. L. 1994 Numerical investigation of receptivity to freestream vorticity. *Phys. Fluids* **6**, 3368–3379.

Davis, R. T. 1972 Numerical solution of the Navier–Stokes equations for symmetric laminar incompressible flow past a parabola. *J. Fluid Mech.* **51**, 417–433.

Erturk, E. 1999 Leading-edge boundary layer receptivity to oblique freestream acoustic waves on parabolic bodies. PhD thesis, Illinois Institute of Technology, Chicago.

Erturk, E. & Corke, T. C. 2001 Boundary layer leading-edge receptivity to sound at incidence angles. *J. Fluid Mech.* **444**, 383–407.

Erturk, E., Haddad, O. M. & Corke, T. C. 2004 Laminar incompressible flow past parabolic bodies at angles of attack. *AIAA J.* **42**, 2254–2265.

Fucciarelli, D. 1997 Numerical simulations of leading-edge acoustic receptivity. PhD thesis, Arizona State University, Tempe.

Gatski, T. B. & Grosch, C. E. 1987 Numerical experiments on boundary-layer receptivity. In *Proc. Symp. on the Stability of Time-Dependent and Spatially Varying Flows*, pp. 82–96. Springer.

Golstein, M. E. 1983 The evolution of Tollmien–Schlichting waves near a leading edge. *J. Fluid Mech.* **127**, 59–81.

Golstein, M. E. 1985 Scattering of acoustic waves into Tollmien–Schlichting waves by small streamwise variation in surface geometry. *J. Fluid Mech.* **154**, 509–529.

Goldstein, M. E. & Hultgren, L. S. 1989 Boundary-layer receptivity to long-wave free-stream disturbances. *Annu. Rev. Fluid Mech.* **21**, 137–166.

Haddad, O. M. & Corke, T. C. 1998 Boundary layer receptivity to free-stream sound on parabolic bodies. *J. Fluid Mech.* **368**, 1–26.

Hammerton, P. W. & Kerschen, E. J. 1992 Effect of nose bluntness on leading-edge receptivity. In *Instability, Transition and Turbulence* (ed. M. Y. Hussaini, A. Kumar & C. L. Streett). Springer.

Hammerton, P. W. & Kerschen, E. J. 1996 Boundary-layer receptivity for a parabolic leading edge. *J. Fluid Mech.* **310**, 243–267.

Hammerton, P. W. & Kerschen, E. J. 1997 Boundary-layer receptivity for a parabolic leading edge. Part 2. The small strouhal number limit. *J. Fluid Mech.* **353**, 205–220.

Lin, N., Reed, H. L. & Saric, W. S. 1990 Leading edge receptivity to sound: Navier–Stokes computation. *Appl. Mech. Rev.* **43**, S175.

Lin, N., Reed, H. L. & Saric, W. S. 1992 The effect of leading edge geometry on boundary layer receptivity to freestream sound. In *Instability, Transition and Turbulence* (ed. M. Y. Hussaini, A. Kumar & C. L. Streett), p. 421. Springer.

Murdock, J. W. 1980 The generation of Tollmien–Schlichting wave by a sound wave. *Proc. R. Soc. Lond.* A **372**, 517–534.

Saric, W. S. & Rasmussen, B. K. 1992 Boundary-layer receptivity: free-stream sound on an elliptical leading edge. *Bull. Am. Phys. Soc.* **37**, 1720.

Saric, W. S., Wei, W. & Rasmussen, B. K. 1994 Effect of leading edge on sound receptivity. In *Laminar–Turbulent Transition IV, Proc. IUTAM Symp. Sendai, Japan* (ed. R. Kobayashi).

Saric W. S. & White, E. B. 1998. Influence of high amplitude noise on boundary-layer transition to turbulence. *AIAA Paper* 98–2645.

Shapiro, P. 1997 The influence of sound upon laminar boundary layer instability. *Acoustics and Vibration Lab. Rep.* 83458-83560-1, MIT.

Wanderley, J. B. V. Corke T. C. 2001 Boundary layer receptivity to freesteam sound on elliptic leading edges of flat plates. *J. Fluid Mech.* **429**, 1–29.